Materials Today Bio 30 (2025) 101384

Contents lists available at ScienceDirect

Materials Today Bio

journal homepage: www.journals.elsevier.com/materials-today-bio

Digital light processing printing of non-modified protein-only compositions

Ayelet Bunin [a,1], Orit Harari-Steinberg [b,1], Doron Kam [a], Tatyana Kuperman [b], Moran Friedman-Gohas [b], Bruria Shalmon [b,c,e], Liraz Larush [a], Shay I. Duvdevani [b,d,e,1,**], Shlomo Magdassi [a,*]

[a] Institute of Chemistry and Center for Nanoscience and Nanotechnology, The Hebrew University of Jerusalem, Jerusalem, 9190401, Israel
[b] Tissue Engineering Research Laboratory, Sheba Medical Center, Tel Hashomer, Ramat-Gan, Israel
[c] Department of pathology, Sheba Medical Center, Tel Hashomer, Ramat-Gan, Israel
[d] Department of Otorhinolaryngology, Head and Neck Surgery, Sheba Medical Center, Israel
[e] Sackler Faculty of Medicine, Tel Aviv University, Israel

ARTICLE INFO

Keywords:
3D printing
Digital light processing (DLP)
Non-modified
di-tyrosine
Cell-laden

ABSTRACT

This study explores the utilization of digital light processing (DLP) printing to fabricate complex structures using native gelatin as the sole structural component for applications in biological implants. Unlike approaches relying on synthetic materials or chemically modified biopolymers, this research harnesses the inherent properties of gelatin to create biocompatible structures. The printing process is based on a crosslinking mechanism using a di-tyrosine formation initiated by visible light irradiation. Formulations containing gelatin were found to be printable at the maximum documented concentration of 30 wt%, thus allowing the fabrication of overhanging objects and open embedded. Cell adhesion and growth onto and within the gelatin-based 3D constructs were evaluated by examining two implant fabrication techniques: (1) cell seeding onto the printed scaffold and (2) printing compositions that contain cells (cell-laden). The preliminary biological experiments indicate that both the cell-seeding and cell-laden strategies enable making 3D cultures of chondrocytes within the gelatin constructs. The mechanical properties of the gelatin scaffolds have a compressive modulus akin to soft tissues, thus enabling the growth and proliferation of cells, and later degrade as the cells differentiate and form a grown cartilage. This study underscores the potential of utilizing non-modified protein-only bioinks in DLP printing to produce intricate 3D objects with high fidelity, paving the way for advancements in regenerative tissue engineering.

1. Introduction

3D bioprinting holds great promise in the field of personalized medicine, including the fabrication of patient-specific implants [1–3]. There are two main approaches to fabricating biological implants: printing a bio-scaffold followed by cell-seeding or printing compositions containing living cells (cell-laden) [4,5].

Protein-based scaffolds offer advantages over conventional materials, providing biocompatible templates for cell adhesion, proliferation, and differentiation in tissue regeneration [6,7]. Cartilage tissue engineering [8] can be performed by *in vivo* implantation, where constructs benefit from the native environment and vascular supply [2,9], or *ex vivo/in vitro* cultivation, allowing controlled laboratory conditions [10–12]. Recent developments focus on scaffolds with tailored architecture, mechanical properties, and bioactive elements to support chondrocyte development and cartilage matrix formation [13,14].

Among 3D bioprinting technologies, Direct Ink Writing (DIW) and stereolithography are leading candidates. While DIW offers accessibility and cost-effectiveness, it faces challenges in resolution and potential cell damage [15–17]. Conversely, stereolithography methods like Digital Light Processing (DLP) achieve superior precision, enabling the fabrication of complex structures with micron to submicron resolution [18–23].

Most bioinks used in DLP consist of one or a combination of two main components: Synthetic monomers, such as acrylamide or poly(ethylene glycol) diacrylate. The second is biopolymers with covalently bonded

* Corresponding author.
** Corresponding author. Tissue Engineering Research Laboratory, Sheba Medical Center, Tel Hashomer, Ramat-Gan, Israel.
E-mail addresses: shay.duvdevani@sheba.health.gov.il (S.I. Duvdevani), Shlomo.Magdassi@mail.huji.ac.il (S. Magdassi).
[1] These authors contributed equally to this work.

https://doi.org/10.1016/j.mtbio.2024.101384
Received 2 August 2024; Received in revised form 18 November 2024; Accepted 4 December 2024
Available online 6 December 2024

reactive groups, such as gelatin-methacrylate (GelMA). However, both approaches rely on synthetic components, which can adversely affect the bioink and the printed structures' biocompatibility and potentially hinder their suitability for biological applications [24]. Currently, only a few publications discuss DLP printing of non-functionalized biopolymers.

Protein-only bioinks offer enhanced biocompatibility and eliminate the need for chemical modifications like methacrylate attachment [21,25,26]. Our research focuses on non-functionalized gelatin, which provides numerous advantages, including biocompatibility, solubility, degradability, cost-effectiveness (~0.7$ per gram versus ~300$ for GelMA), and reduced antigenicity compared to collagen [27]. Gelatin's established safety profile in food industry applications [28] and medical devices, including drug delivery systems [29], makes it particularly attractive for regenerative tissue engineering and wound healing applications [30].

Importantly, gelatin contains the arginine-glycine-aspartic acid (RGD) peptide sequence, promoting cell adhesion, proliferation, and differentiation—crucial factors for effective bioscaffold development [31]. Recent research has highlighted gelatin's potential in cartilage tissue engineering, as it effectively mimics the extracellular matrix (ECM) of native cartilage tissue [32,33]. Advanced fabrication techniques enable the creation of organized porous scaffolds with controlled properties supporting cellular functions [32,34].

3D printing of gelatin solutions faces challenges, including gelation, while used at high concentrations that are required for solidification. Printing chemically modified gelatin (e.g., GelMA) requires water-soluble photoinitiators (PIs), which have limited availability and efficiency [35,36]. On the other hand, non-modified gelatin can undergo photopolymerization to form di-tyrosine bonds using a water-soluble PI component – ruthenium complex with sodium persulfate (Ru/SPS) [25,37]. The Ru/SPS system enables crosslinking of native gelatin when exposed to light within the visible spectrum (400–700 nm), avoiding UV light's potential for DNA mutations and chromosomal instability that can lead to reduced cell viability [38]. The Ru(bpy) complex has an absorbance peak at 452 nm [39], but importantly, it maintains sufficient absorbance at 405 nm, a wavelength commonly used in commercial DLP printers, as successfully performed by Soliman et al. [40].

Upon irradiation, the Ru(II) complex with persulfate undergoes photolysis, producing Ru(III) and sulfate radicals. The Ru(III) acts as an oxidizing agent, forming tyrosine radical intermediates that couple with nearby tyrosine groups, stabilized by persulfate radicals [25]. While this reaction shares similarities with commonly known free radical photo-polymerization processes, such as light-triggered initiation and the formation of radical species, the Ru/SPS di-tyrosine crosslinking mechanism differs in several key aspects. Firstly, in typical photo-cleavage-based reactions, the photoinitiator itself transforms into a radical form upon light irradiation and directly attacks a nucleophilic group in the monomer (usually a double bond). In contrast, the Ru/SPS system involves a more complex electron transfer process where Ru(II) is oxidized to Ru(III), which then oxidizes tyrosine residues. Secondly, common photo-polymerization reactions are often chain reactions propagating through the material. The di-tyrosine crosslinking, however, is more localized, involving the coupling of neighboring tyrosine residues. Lastly, the Ru/SPS system doesn't introduce new chemical entities into the protein structure, preserving the biocompatibility of the original material. Lim et al. demonstrated that Ru/SPS offers advantages over conventional PIs like Irgacure 2959, showing reduced oxygen inhibition and maintaining ~90 % cell viability even at high light intensities (100 mW cm-2), while Irgacure 2959's cell viability drops to ~45 % [41]. Despite its higher cost, the Ruthenium complex requires a significantly lower concentration (0.06 wt%) compared to common water-soluble PIs like LAP (~0.5–1 wt%), making it approximately ten times more cost-effective [42].

To the best of our knowledge, the utilization of pristine protein-only photopolymerization-based 3D printing has been reported in only a few publications, each employing a different technique. We previously reported successfully printing resilin protein using a two-photon printing approach. [43], which resulted in small-scale scaffolds, typically on the micron scale, under high-intensity irradiation. Xie et al. printed silk-based proteins only by Volumetric Additive Manufacturing (VAM) [44], a compelling 3D printing technique still in its nascent stages of development. Two additional reports on printing proteins only were introduced about keratin [45] and silk fibroin [46] printed in DLP using riboflavin as a PI, with very long irradiation times, 3–4 min per layer. Another recent relevant publication by Soliman et al. employed pristine gelatin in a bulk hydrogel as a delayed sacrificial ink [40], where gelatin and Ru/SPS formulations were irradiated in different 2D structures by a DLP printer, similar to what can be achieved by soft lithography processes. Previous works have explored di-tyrosine reactions in gelatin but were limited to molding techniques [37], extrusion-based 3D printing [47], or the use of modified proteins such as GelMA [41,48,49]. Our approach uniquely combines the di-tyrosine reaction of non-modified gelatin with commercial DLP printing in a single step, representing a significant advancement in protein-based 3D printed hydrogels.

This study presents novel DLP 3D printing compositions that utilize only non-modified gelatin to fabricate complex 3D structures for applications such as cartilage. The crosslinking mechanism relies on irradiation at visible light, which is not harmful to the cells. Both cell-seeding and cell-laden approaches were evaluated, and preliminary biological experiments indicate the potential of the gelatin scaffolds in making high-resolution cartilage implants.

2. Materials and methods

2.1. Materials

Gelatin from porcine skin – type B, $[Ru(bpy)_3]^{+2}$, Tartrazine, and sodium phosphate (dibasic and monobasic) were purchased from Sigma Aldrich. Sodium persulfate (SPS) was purchased from Holland Moran, Israel. Phenol red was purchased from Acros Organics.

2.2. Bioink preparation

Phosphate buffer saline (PBS) was prepared according to standard protocol [28]. Gelatin (30 or 22.5 wt%) was dissolved in PBS and heated to 50 °C while stirring. Concentrated solutions of 40 mM $[Ru(bpy)_3]^{+2}$ and 400 mM SPS were diluted to a final concentration of 0.8 and 8 mM, respectively. Solutions of 0.1 wt% were made for each photo-absorber and were diluted to 0.01 wt% in the final ink composition (0.28 mM of Phenol-red and 0.19 mM of Tartrazine).

2.3. Fabrication of 3D structures in mold

UV-curable solution was poured into a mold and irradiated for 60 s with a 405 nm UV torch (32 DC V, 8 A).

2.4. DLP printing

A predesigned CAD printed model was generated using a DLP printer (Asiga Max X35, Australia) equipped with a 405 nm LED. The printer's XY-axis resolution is 35 μm, while the maximum resolution on the Z-axis is down to 1 μm. The printing composition was poured into the designated heating bath heated to 50 °C. Each printed layer was 100 μm thick and was cured for 35 s with a light intensity of 7.5 mW cm^{-2}. The resulting printing rate is 1cm/50min (height). All printing experiments (excluding cell-laden ones) include a thorough washing stage. The vat was heated to 45 °C for printing without cells, followed by a post-printing washing stage until complete dissolution of the unpolymerized portion (water at 85 °C for 5–10 min). For the cell-laden printing experiments, the vat was maintained at 37 °C during printing, followed by a post-printing rinsing stage, until the full dissolution of the

unpolymerized portion (PBSx1 with 1 % Penicillin-Streptomycin and 0.1 % Amphotericin B, at 37 °C, 3–5 times, each for 5 min). Both scaffold types were then sequentially washed six times for 5 min each, in PBSx1 with 1 % Penicillin-Streptomycin and 0.1 % amphotericin B solution on a shaker at 37 °C. The 3D objects STL files were obtained from Thingiverse, Anatomical heart by airforce (https://www.thingiverse.com/thing:942464, license: CC-BY-SA), 3D Benchy by Creative-Tools (https://www.thingiverse.com/thing:5293974, license: CC-BY-ND). All other STL files were designed with Autodesk Inventor software.

2.5. Electron microscopy

Scanning Electron Microscope (XHR-SEM) images were obtained using an extra-high-resolution scanning electron microscope (XHR Magellan 400 L).

2.6. UV–Vis spectrophotometry

UV–Vis spectrophotometry was used to quantify the ink components' absorption. Spectrophotometric measurements were recorded using a UV-spectrophotometer (UV-1800; Shimadzu, Japan). Absorption spectra of ink components (gelatin, gelatin with PI, and gelatin with PI and various dyes) were recorded in the spectral range of 300–800 nm with a resolution of 0.5 nm.

2.7. Fluorescence spectroscopy

Steady-state fluorescence measurements were performed on a HORIBA JOBIN YVON Fluoromax-4 spectrofluorometer with the excitation/emission geometry at right angles. A thin film of the ink formulation was applied to a quartz slide, and fluorescence measurements were taken before and after irradiation (excitation at 285 nm, emission spectrum recorded from 300 to 500 nm).

2.8. Compression test

For the compression test, discs (10 mm in diameter and 5 mm thick) were printed using bioinks and washed with water at 85 °C for 5 min. Each printed model's diameter and thickness were measured at three different areas, and the reported values are the averages.

Compression mechanical tests of the obtained discs were performed on the fully cured samples using an Instron universal testing machine (Model 3345, Instron Corp., Norwood, MA) equipped with a 500 N load cell. The compression test was conducted at 25 °C using 10 mm min-1 crosshead speed.

2.9. Tensile test

For tensile test, dogbone-shaped samples (15 × 5 × 3 mm) were printed using bioinks and washed with water at 85 °C for 5 min. Each printed model's length, width, and thickness were measured at three different areas, and the reported values are the averages. Tensile mechanical testing was conducted using an Instron Universal Testing machine (Model 3345, Instron Corp., Norwood, MA) equipped with a 500N load cell, at a rate of 10 mm min−1. The reported value is the average of the five printed models. Young's modulus was calculated using the slope of the linear portion of the curve, corresponding to the material's elastic region.

2.10. Dynamic mechanical analysis

Discs with a nominal sample size of 10 × 5 mm (diameter x height) were printed to evaluate DMA properties. Rheometer (RheoStress HAAKE 6000) was used with a parallel plate geometry (P35 Ti L – 60 mm) at 25 °C. Oscillation Amplitude Sweep (OAS) was carried at a frequency of 1 Hz, and a range of shear stresses of 0.1–1000 Pa was tested. The gap between the plates was set to fit 1.5 N.

After identifying the Linear Viscoelastic Region (LVER) from the OAS tests, the desired shear stress (Tau) for later assays was chosen. Oscillation Frequency Sweep (OFS) was carried at shear stress of 1 Pa for frequencies of 0.1–100 Hz. The gap between the plates was set to fit 1.5 N.

2.11. Cell isolation and expansion

Tissue sample collection was approved by the Sheba Medical Center Ethics Committee (4745–17-SMC). All patients signed consent forms. Chondrocytes were isolated from nasal cartilage as previously described by our group [10]. In brief, nasal cartilage was cut into 1–3 mm pieces, incubated with collagenase II for 12–14 h, and washed with growth medium (DMEM/F12 with 10 % fetal bovine serum and 1 % pen-strep) following a 100 μm strainer filtration. After being centrifuged at 600×*g* for 8 min, the cells were cultured with growth medium replacement every 2–3 days until reaching a confluence of 80 %.

2.12. Chondrocyte seeding onto printed gelatin scaffolds

Chondrocytes in passage two were trypsinized (0.25 % trypsin - biowest) and washed with a growth medium. Following cell count, the supernatant was gently aspirated, and the pellet was suspended (30 μL of 8 % gelatin at 37 °C) and seeded drop-wise onto the gelatin scaffolds at a cell concentration of 15-30x104/μL. The seeded scaffolds were incubated at 37 °C in a humidified atmosphere of 5 % CO2 in air in a growth medium and replaced every 2–3 days.

2.13. Viability and proliferation analysis within constructs

RealTime-Glo™ MT Cell Viability Assay (Promega) was performed according to the manufacturer's instructions. The assay uses a cell-permeant luciferase substrate and a cell-impermeant oxidoreductase enzyme. This enzyme is only active in metabolically active cells. When the enzyme reduces the substrate, it produces a luminescent signal that is proportional to the number of viable, metabolically active cells. Luminescence was measured using a GloMax plate reader (Promega).

CellTiter 96® Non-Radioactive Cell Proliferation Assay (MTS) (Promega) was performed according to the manufacturer's instructions. The assay uses a tetrazolium compound called MTS (3-(4,5-dimethylthiazol-2-yl)-5-(3-carboxymethoxyphenyl)-2-(4-sulfophenyl)-2H-tetrazolium). This compound is bioreduced by cells into a colored formazan product that is soluble in the culture medium. As measured by the absorbance at 490–500 nm, the amount of formazan produced is directly proportional to the number of living cells. Absorbance was measured using a GloMax plate reader.

FDA-PI (Fluorescein Diacetate - Propidium Iodide) staining live/Dead assay: Dyes solution of FDA (Sigma F7378): 1:500 dilution and PI (Sigma P4864) 1:150 dilution was added to the samples followed by incubation for 10 min. FDA is a non-fluorescent compound that can freely permeate live cell membranes. Once inside the cells, intracellular esterases cleave the diacetate groups at 37 °C, releasing fluorescein, which then emits green fluorescence. Samples were imaged using a light inverted microscope (Olympus IX83, Olympus, Japan) or measured using a GloMax plate reader (Promega).

2.14. Viability and proliferation analysis of chondrocyte cultures

Cells were collected from the gelatin ink formulation before and after printing, seeded in triplicate at 3000 cells/well density in 96-well plates, and incubated in a growth medium. Culture viability was analyzed using RealTime-Glo assay and FDA/PI staining or counted using the trypan blue exclusion staining. Cells were mixed with Trypan Blue (Biological Industries) at a 1:1 ratio. Live and dead cells were counted using a CellDrop BF Bright Field cell counter (DeNovix).

2.15. Histology and immunostaining

After 7 days of culture, cell-seeded scaffolds were fixed (4 % formaldehyde) for 24 h and embedded in paraffin at 65 °C. The scaffolds were sectioned at 5 μm thickness, deparaffinized with OmniPrep solution (ZytoMed) for 40 min at 80 °C, rehydrated, and stained with hematoxylin and eosin (H&E) for morphological analysis. For immunostaining, sections were permeabilized, washed with PBS, and blocked with BSA solution for 1 h. Sections were then incubated with a Ki67 primary rabbit monoclonal antibody (1:300, ePredia by Fisher Scientific) according to the manufacturer's instructions, mounted, and imaged using a light inverted microscope (Olympus IX83, Olympus, Japan).

2.16. Statistical analysis

Statistical analysis was performed using a two-tailed unpaired Student's t-test. Differences between groups were considered statistically significant when the p-value was ≤0.05. P-values symbols legend:

>0.05	ns
≤0.05	*
≤0.001	**
≤0.0001	***
≤0.00001	****
≤0.000001	*****
≤0.0000001	******

3. Results and discussion

3.1. Ink formulation and optimization

Gelatin is considered a thermo-responsive material, as it undergoes a reversible sol-gel transition between solution (known as "sol" phase) and amorphous solid (known as "gel" phase). This process results in significant changes in the viscoelastic properties of the material, making it an important factor in view of printability and workability since the mobility of the reacting molecules is an essential factor for the polymerization process [50]. A series of gelatin printing compositions was prepared to test the suitability for the printing process by irradiating samples in a mold at 405 nm. It should be noted that although the peak of the ruthenium complex is at 452 nm, it has sufficient absorption at 405 nm, which is common for commercial printers (Fig. S1). Upon irradiation, it was found that the polymerized gelatin, at concentrations below 10 wt% gelatin, did not maintain its original shape after polymerization. The structural integrity depends on the crosslinking density, which can be evaluated by determining the cross-over point [51–53]. It is the intersection between the storage and loss moduli, as measured by Oscillation Amplitude Sweep (OAS) tests. The results showed a significant increase in the crossover point from 300 Pa for 10 wt% gelatin to 2800 Pa for 22.5 wt% gelatin, indicating a general trend of enhanced crosslinking density and mechanical stability at higher concentrations.

Conversely, formulations with gelatin concentrations exceeding 15 wt% required high temperatures to be printed due to the high viscosity at room temperature. At a gelatin concentration of 30 wt%, a printing temperature of around 45 °C was found to be optimal.

The elevated temperature during printing (45 °C) causes the denaturation of the gelatin, resulting in a random coil tertiary structure [54]. As gelatin is a linear protein, its tertiary structure is inherently simple. Importantly, the primary structure of gelatin remains stable up to 70 °C [55,56], ensuring its integrity throughout the entire printing process.

Notably, the ink formulation also included SPS, which undergoes thermal activation above 70 °C for an extended duration [57], and therefore, a practical upper limit of 30 wt% gelatin was selected for the subsequent printing experiments. Preliminary experiments were conducted to optimize the Ru/SPS concentrations, as the ratio between the two components was maintained at 1:10, as described in several publications [19,48,49,58]. The effect of the concentration of Ru/SPS on the crosslinking density was evaluated by cross-over point determination. As shown in Fig. S2, the results revealed that a concentration of 0.8/8 mM Ru/SPS effectively balances sufficient crosslinking with a minimal use of the photoinitiator. Higher concentrations did not significantly change the crossover point, indicating that they lead to similar crosslinking densities.

The rheological properties of three gelatin solutions are presented in Fig. S3, supplementary information). As expected, higher concentration led to higher viscosity. Interestingly, a hysteresis loop was observed during the measurements, which involved two measurement stages: heating from 10 °C to 60 °C, followed by a cooling stage back to 10 °C. Because of this hysteresis, the gelatin solutions were prepared at a high temperature, 65 °C, while the printing experiments were performed at 50 °C.

The printing experiments were performed according to the scheme presented in Fig. 1. In essence, the protein solution contained the Ru/SPS initiator, placed in the heated DLP vat, and irradiated at 405 nm via a layer-by-layer process, according to the sliced CAD file. The resulting object is a crosslinked hydrogel rinsed off with water (80 °C) to remove all unreacted gelatin.

3.2. Optimization of printing parameters

When fabricating each layer by the DLP process, the depth to which the light beam penetrates the resin critically governs each voxel dimension. As established by Jacobs, the cure depth can be expressed by the following relationship [59]:

$$Equation\ 1: \quad Cd = D_p \bullet ln(E/E_c)$$

Where Cd – cure depth, Dp – penetration depth, E – energy dosage, Ec – critical energy. It is important to note that the energy dosage is the product of light intensity, given in units of mW cm^{-2}, and the exposure time in seconds [60].

The cure depth of various formulations was evaluated by irradiation within the DLP vat at given energy doses and by measuring the thickness of the cured layer with an optical microscope. Fig. 2A shows the cure depth as a function of exposure time for two light intensities. As seen, increasing the exposure time led to increased thickness for both light intensities, leveling off at the higher intensity and long irradiation duration. As shown in Fig. 2B, the cure depth of formulations without a dye and with Phenol red and Tartrazine were linearly dependent on the natural logarithm of the energy. According to Jacob's working curve, the curve's slope represents the formulation's penetration depth, while the y-intercept corresponds to the critical energy required for polymerization. Interestingly, the critical energy for the composition without a dye was 28.8 mJ cm^{-2}, compared to 38.1 mJ cm^{-2} and 154.4 mJ cm^{-2} for compositions containing Tartrazine and Phenol red, respectively.

The curing depth was determined for several theoretical light intensities, and the results were plotted as a function of exposure time (Fig. 2C). Utilizing the linear equation derived from the working curve, these trends were calculated, with a fixed light intensity chosen for each trend. This analysis enabled the identification of a specific light intensity that would allow easy tuning of the cure depth while maintaining short printing times. As seen in Fig. 2C (inset), at high light intensities, the slopes are steep, thus predicting significant changes in cure depth upon minor changes in exposure time. Conversely, lower intensity levels require printing times that are too long. Therefore, we selected irradiation of 7.5 mW cm^{-2} for which the cure depth is not very sensitive to irradiation time, and yet it enables printing in short durations, ~40 s. Confining the polymerization area to small spots is crucial to achieve a high dimensions similarity between the CAD file and the printed object. This can be accomplished by employing photo absorbers (dyes) that can absorb a certain amount of light without causing polymerization. For bioprinting applications, selecting appropriate dyes becomes crucial, as

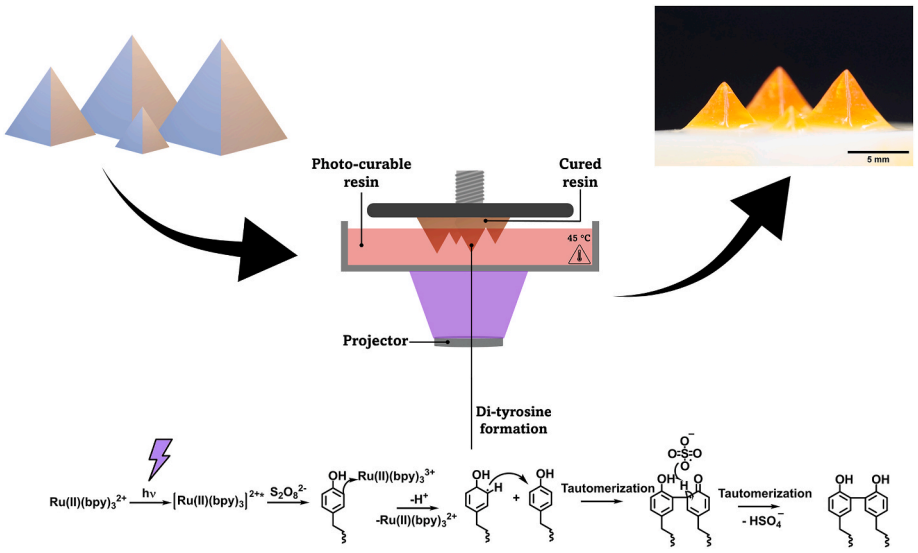

Fig. 1. Schematic presentation of the DLP printing process for non-modified protein-only ink. The procedure commences with the design of a CAD file, subsequently fed into slicing software that translates the 3D CAD design into a sequence of 2D patterns. These patterns are projected onto the photocurable ink, directing the initiation of a photo-chemical di-tyrosine reaction at specific locations as dictated by the pattern.

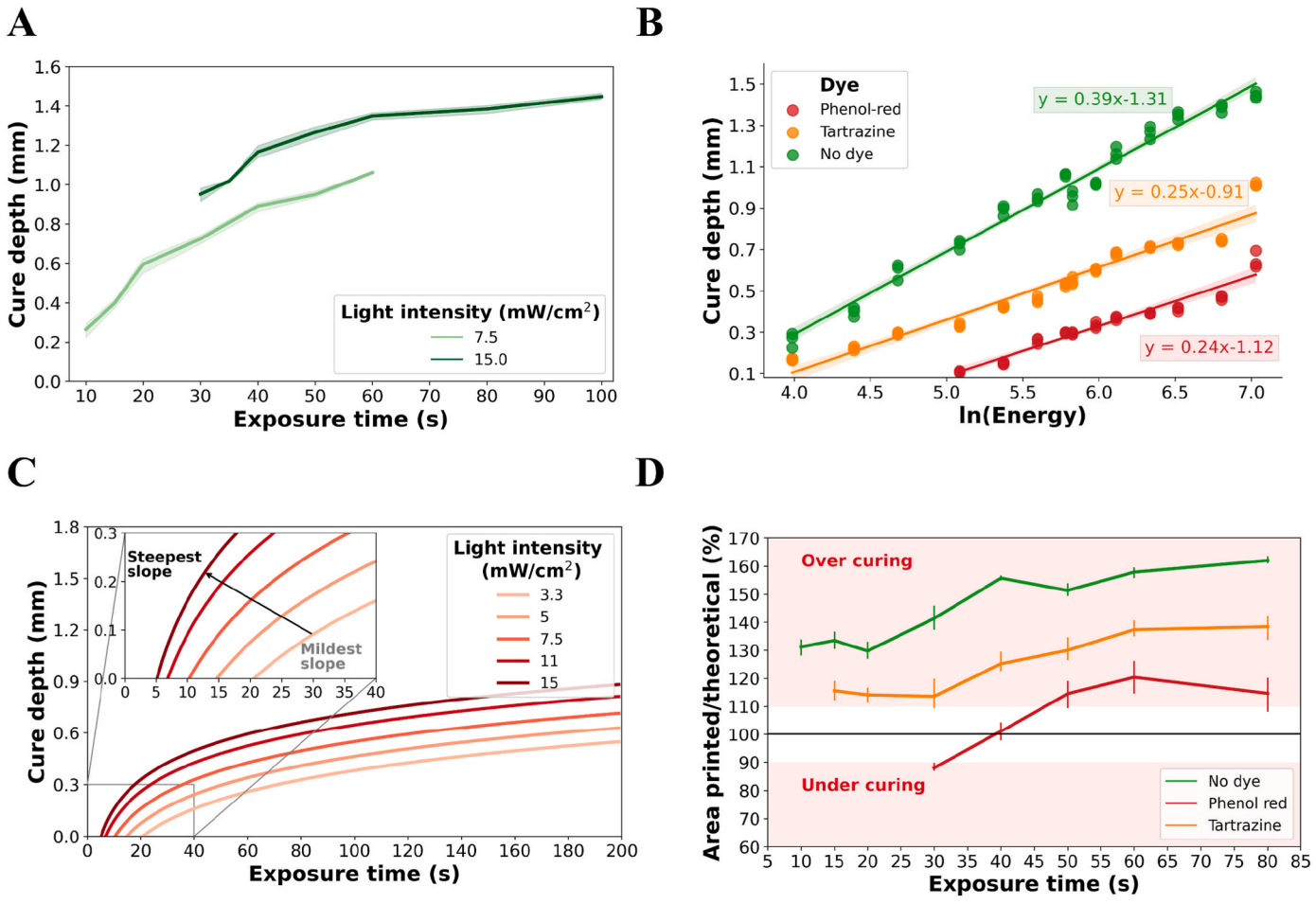

Fig. 2. Cure depth analysis enables a deeper understanding and better customization of the printing parameters. (A) Cure depth measurements for ink formulation without dye for two light intensities (3 reps). (B) Linear trends were observed for each formulation's cure depth, which correlates with the natural logarithm of the energy (N = 3). (C) Calculated cure depth was determined for a range of light intensities as a function of exposure time. (D) XY-resolution test shown by area printed/theoretical (%) for each formulation at various exposure times were evaluated for each formulation (without dye, with Tartrazine, and with Phenol red). 100 % resemblance is shown as a black line. All error bars represent confidence intervals (95 %). (For interpretation of the references to color in this figure legend, the reader is referred to the Web version of this article.)

they should absorb the specific wavelength and yet be non-harmful to living systems. Phenol red emerges as a promising candidate for the intended application due to its absorption characteristics around 400 nm and its frequent use in cell culture media. It has a very low toxicity, excellent stability within living systems, and minimal interference with biological processes [61]. Tartrazine, another pertinent dye, has been employed in diverse cell-related systems, serving as a coloring agent in food and cosmetic products [62]. Fig. S1 shows that formulations containing these dyes exhibit stronger absorbance at the relevant wavelength of the printer (405 nm), making them suitable choices for investigation as potential resolution enhancers in the ink formulation. The UV–Vis spectra of the various solutions are presented in Fig. S1, along with the printer's irradiation peak and intensity. As described above, the critical energy of polymerization was the highest for Phenol red, 154.4 J cm^{-2}. Thus, it should be very effective in controlling resolution, and therefore, the subsequent experiments were performed with this dye.

Different dyes affect the resin's curing depth in various ways due to their distinct absorption characteristics at the DLP printer's operating wavelength [63]. As shown in Fig. S1, phenol red displays higher absorption in the relevant wavelength range, which helps to confine the polymerization reaction to the selected pixel and reduce light scattering effects [64]. Additionally, energy transfer can occur within the system, primarily from the Ruthenium complex to phenol red. This further contributes to a more localized reaction, preventing over-curing and resulting in a higher resolution [65]. In contrast, the Tartrazine formulation facilitates energy transfer in the opposite direction, from the dye to the Ruthenium complex [66]. While this enhances the reaction, it may also lead to the over-curing of the fabricated object. Given that our main goal in adding a dye is to achieve higher resolution, phenol red was determined to be more suitable for our purposes. This preference is reflected in the critical energy value, representing the energy threshold required to initiate the reaction. Furthermore, such formulations are susceptible to extensive polymerization along the z-axis, resulting in over-curing in this dimension. The relationship between print speed and resolution presents a significant parameter in optimizing the printing process. Formulations with higher critical energy, such as the phenol red-based mixture used in this study, require longer exposure times. While beneficial for achieving higher resolution, this increased exposure time impacts the overall print speed.

The XY resolution was evaluated by printing rectangles and comparing their dimensions to the corresponding CAD file. This assessment involved measuring the area of each printed rectangle using ImageJ software. Fig. 2D shows the % area printed/theoretical area for each formulation at various exposure times, while 100 % is defined as the highest resolution. Above 100 % is termed overcuring, and below 100 % is termed under-curing. In general, as expected, the higher the exposure time, the larger the printed area compared to the designed area. The formulations without dye and with Tartrazine were always overcured (and at lower exposure time, did not cure at all).

In comparison, the formulation containing Phenol red was either over-cured or under-cured, while at 40 s of exposure, the ratio was 100 %, meaning excellent resolution. Therefore, the subsequent printing experiments were performed at the same irradiation energy (300 mJ cm^{-2}). These experiments were under irradiation intensity, meaning that in view of energy, the irradiation time can be shortened by increasing the intensity.

3.3. 3D printed models

By using a gelatin concentration of 30 wt%, simple shapes could be 3D printed, e.g., pyramids shown in Fig. 1. We conducted fluorescence spectroscopy analysis to further validate the formation of di-tyrosine bonds and distinguish between physical gelation and photo-crosslinking. The resulting spectra (Fig. S4) show an increase in emission intensity around 400–410 nm after irradiation, consistent with di-tyrosine bond formation [67]. However, it is important to note that due to the complex nature of gelatin, which contains tyrosine residues within a large molecule with many chemical entities, the fluorescence spectrum presents a broad peak rather than a sharp, easily quantifiable signal known for small molecules. This complexity limits the ability to perform precise quantitative analysis of the crosslinking reaction based solely on fluorescence intensity differences. These results, combined with the thorough washing protocol at 85 °C, which dissolves any uncrosslinked or physically gelled gelatin, provide strong evidence for the successful photo-crosslinking of the gelatin-based ink. However, for more complex structures, it was found that it was necessary to decrease the gelatin concentration. After evaluating various concentrations, a 22.5 wt% was selected, enabling printing structures as shown in Fig. 3. Interestingly, the printed hydrogel structures were stretchable, as seen in Fig. 3B and videos S1 and S2 in the supplementary information. Another noteworthy feature of the printed gelatin structures is their response to pH change, in view of swelling and color, which makes the object classified as 4D printed. The printed structures were immersed in aqueous solutions having various pH values. As seen in Fig. 3D, the objects swell with the increase in pH, with higher pH values leading to more substantial swelling. The swelling increases by ~140 % while immersed at pH 12 compared to pH 4. This phenomenon results from the deprotonation of the gelatin (type B, isoelectric point of 4.5) [68] as the gelatin molecules are crosslinked.

The use of Phenol red as a dye also enables color and response while the pH is the stimuli, as shown for other 4D printed objects [69,70]. At pH 4, the hydrogel containing Phenol red displayed a yellow color, and as the pH increased, the hydrogel transitioned to a solid red appearance at pH 12. This pH-dependent color shift further highlights the potential use of colorants, including PR, in bioprinting applications at which pH monitoring or visual detection is essential, such as wound healing applications [71,72].

Once the optimal composition and printing parameters are defined, printing hydrogel structures with high complexity is realized. As presented in Fig. 3, these printing compositions enabled the fabrication of overhanging structures and objects with embedded, open tubings, which are essential for bioprinting implants with blood vessels.

The addition of photo-absorbers plays a crucial role, particularly in fabricating tubular structures. These additives absorb some of the irradiated light, effectively confining the crosslinking reaction to smaller, more precisely defined areas. This confinement is especially important along the z-axis when creating open tubes. In the z-axis, the photo-absorbers enable the polymerization to occur up to a specific depth while leaving subsequent layers unpolymerized. This controlled cure depth is essential for forming the open part of the tube. Without photo-absorbers, the light could penetrate too deeply, resulting in solid structures rather than hollow tubes. The use of photo-absorbers must be combined with careful optimization of light irradiation energy. This optimization ensures that the resin absorbs enough energy to initiate and sustain the crosslinking reaction while preventing overcuring, particularly along the z-axis. Achieving the right balance between photo-absorber concentration and light energy is crucial. If there is too little energy, the polymerization process may be incomplete, resulting in mechanically weak structures. Conversely, excessive energy can cause overcuring and compromise the structural integrity, particularly when creating hollow features. This delicate balance between photo-absorbers and light energy allows for precise control over the geometry and the mechanical properties of the printed tubular structures.

It's noteworthy that the majority of existing research in DLP printed hydrogels commonly uses proteins with covalently bonded polymerizable groups or compositions, including synthetic monomers. Conversely, prior published works employing protein-only formulations typically encompass much lower protein concentrations than our current research, a feature that can significantly impact biocompatibility aspects. Fig. 3G presents the published work with DLP printing of proteins, showing that there are only a few non-modified ones, while we use

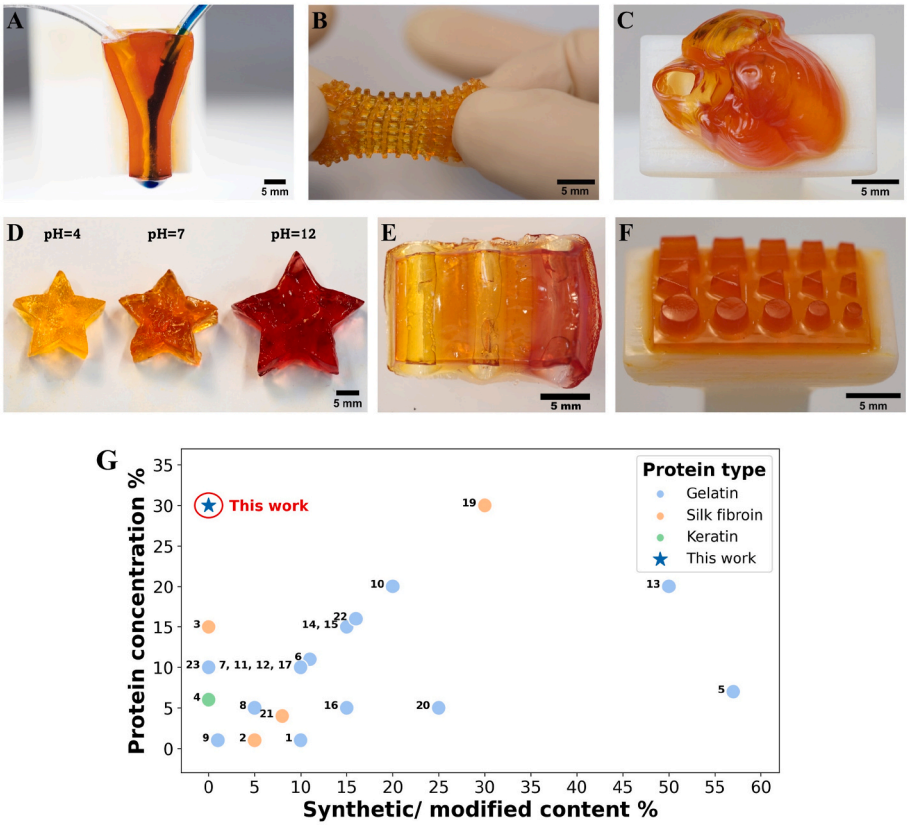

Fig. 3. The suggested formulation utilizes only unmodified gelatin, allowing for relatively high protein concentration DLP printing of objects with different complexities. (A) Y-shaped pipes with two different colorant solutions, (B) stretchable woodpile, (C) Anatomical heart model, (D) Phenol red has the unique property of pH-dependent color change, (E) stretchable network-shaped printed hydrogel, (F) different geometrical objects, and (G) Published works about DLP printing of proteins (full references table in the Supplementary material). (For interpretation of the references to color in this figure legend, the reader is referred to the Web version of this article.)

the highest reported concentration of non-modified protein.

3.4. Mechanical properties of printed structures

To fabricate the 3D cartilage scaffold, it is essential to tailor the material's mechanical properties for soft tissue to facilitate the growth and proliferation of cells, which later degrade as the cells differentiate and form grown cartilage. The mechanical characterization of the printed structures followed two main paths. Initially, the focus was on how the hydrogel behaves under unconfined compression.

Compression tests were chosen for mechanical characterization as they are generally considered more accurate for describing hydrogel mechanical properties. Hydrogels exhibit a pronounced tension-compression asymmetry, where their mechanical response under compression can differ significantly from tension, often by two orders of magnitude in terms of Young's modulus [73]. This asymmetry makes compression tests particularly useful for characterizing the mechanical integrity of hydrogels, which is crucial for applications such as biomedical implants [74]. Fig. S5 shows the results of tensile tests, demonstrating this asymmetry phenomenon. The high variability in the tensile test results makes it unsuitable to consider this test statistically reliable for our hydrogel system.

Eight printed discs underwent a compressibility test, revealing a compression modulus of 31 kPa (Fig. 4A). The printed objects have a modulus similar to soft tissues and within the range of printed GelMA [75]. As a result, it is a suitable candidate to serve as a spatial guiding scaffold for tissue growth. The second approach involved oscillatory measurements, including amplitude and frequency sweeps. The storage and loss moduli obtained from the measurements at the linear viscoelastic region are shown in Fig. 4B and Fig. S6. The storage modulus was 132.97 ± 1.23 Pa, while the loss modulus was 99.02 ± 1.25 Pa. These values are consistent with the trends observed in the earlier compression tests discussed in this section, providing a coherent characterization of the material's mechanical properties.

3.5. Biological studies

Cell adhesion and growth onto and within the gelatin-based 3D constructs were evaluated by examining two cell fabrication techniques: (1) Cell-seeding onto the woodpile-printed gelatin scaffold and (2) printing compositions that contain living cells during the printing process (cell-laden). In the first approach, the cells are not exposed to light irradiation, and the cell growth occurs upon attachment on the woodpile bars of the scaffold and continues to the voids. In the second approach, the cells are exposed to light irradiation and embedded within the gelatin matrix as the printing proceeds. Therefore, the cell growth, in this case, occurs within the polymeric network and continues to the voids between the woodpile bars. Cell survival may be impacted by both deficient adhesion conditions and irradiation. However, we use light within the visible spectrum, which should not be harmful to the cells.

3.5.1. Cell-seeding approach

Using this approach, it was found that chondrocytes seeded onto the 3D printed gelatin scaffolds showed adhesion, survival, and proliferation over 7 days of immersion in culture media.

Cultured human nasal chondrocytes were suspended in 8 % gelatin to enhance initial adhesion and then applied onto the printed scaffolds, followed by incubation in growth media. Bright-field imaging and H&E

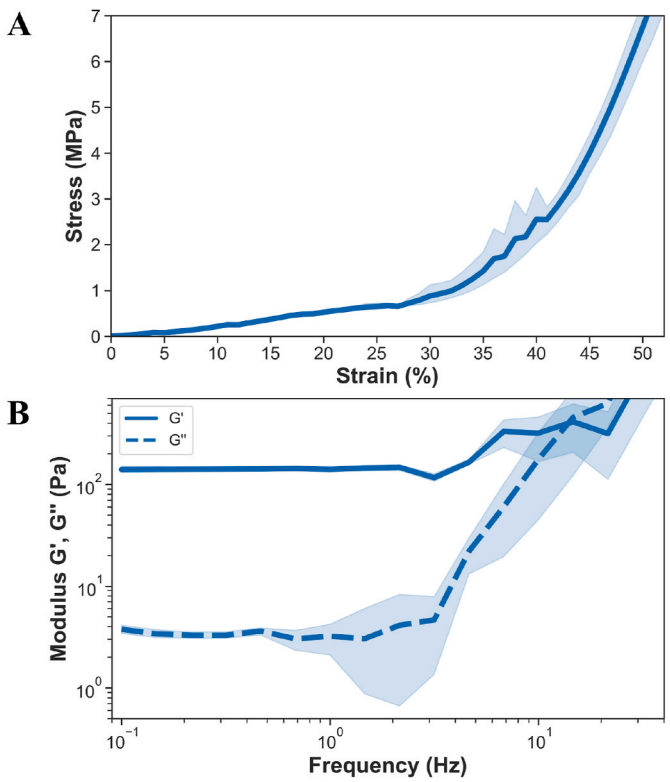

Fig. 4. Mechanical properties examination. (A) stress-strain curve for printed discs (8 reps); (B) oscillatory frequency sweep (OFS) results for printed discs (5 reps). Both storage and loss modulus remained constant for frequencies between 0.1 and 2 Hz. Error bars represent confidence intervals (95 %).

histological analysis showed that chondrocytes adhered to the surface of the scaffold, as shown in Fig. 5A and B. A cell viability assay indicated that viable cells were present at days 5 and 7 post-seeding, as shown in Fig. 5C. The viability of the cells was also confirmed by Live/Dead staining, depicted in Fig. 5D and Fig. S7A. Additionally, Ki67 immunostaining confirmed the presence of proliferating chondrocytes distributed throughout the scaffold after 7 days, as shown in Fig. S7B. These results demonstrate that the 3D printed gelatin scaffolds effectively support chondrocyte attachment and growth following seeding.

3.5.2. *Cell-laden approach*

In this part of the research, the cells were dispersed within the printing formulation. This was followed by a 3D printing process in which the cells were exposed to light irradiation and the mechanical forces occurring during printing. In general, it was found that chondrocytes remained viable, and the cell growth continued within the printing composition and after the printing process. Microscopy imaging showed the presence of embedded chondrocytes within the cell-laden constructs 4 days after printing (Fig. S8A and Fig. S8B). To evaluate the effect of the duration of the printing process on cell survival and proliferation, the printing was performed for 12 or 18 min, and the cells were subsequently cultured for viability analysis. The cell viability assay was performed at 24, 48, 72, and 96 h, and no significant difference in viability was observed between the two printing durations, indicating similar proliferation capacity of the two groups (Fig. S8C and Fig. S8E). Trypan blue staining at day 7 further confirmed that cell viability and proliferation were maintained after the printing process, demonstrated by the fold change from the time zero (original cell culture) (Fig. S8D and Fig. S8F). It is worth noting that the fold change of all tested groups is close to 1 or higher, providing further confirmation that the cells were able to continue proliferation after the suspension in the ink formulation and the printing procedures.

To ensure high cell survival rates, minimizing phototoxicity and maintaining a consistent temperature of 37 °C, particularly during

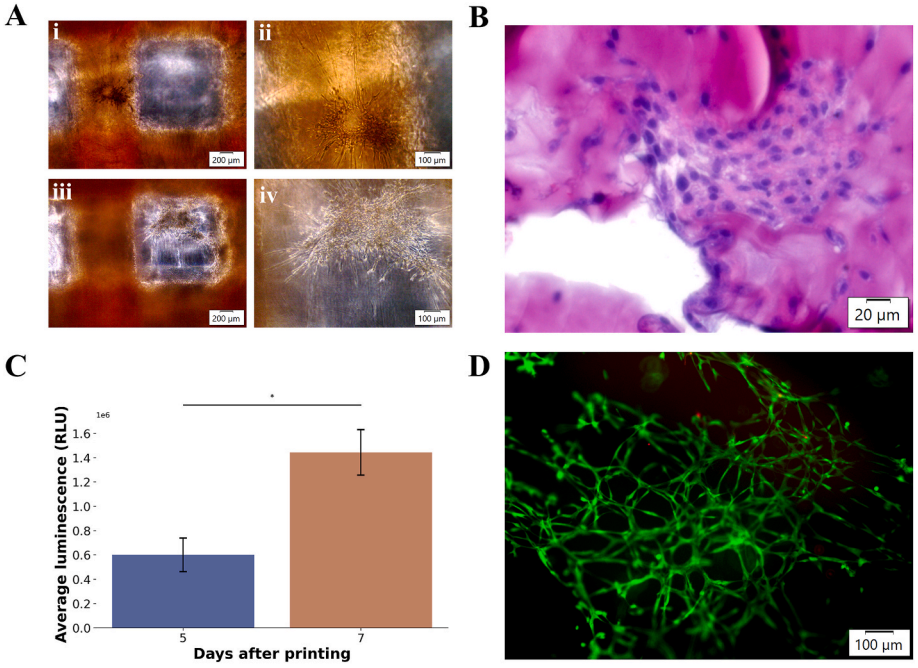

Fig. 5. Chondrocyte viability and growth within 3D printed cell-seeding constructs. Chondrocytes were seeded onto the 3D printed scaffolds in a gelatin solution and grown in cell culture media for up to 7 days. (A) Bright-field microscopy images show cell attachment both on the surface (i, ii) and within the interior voids (iii, iv). (B) Cells within the constructs are shown by H&E histological staining. (C) Cell viability assay demonstrates cell survival and proliferation 5 and 7 days following chondrocytes seeding onto the printed scaffold, N = 1, triplicate. Error bars represent standard deviation. (D) Overlayed microscopy image of Live (green)/Dead (red) dual staining performed with FDA/PI shows high cell viability rates. (For interpretation of the references to color in this figure legend, the reader is referred to the Web version of this article.)

extended printing sessions, is crucial. To overcome these challenges, we used the 'MONO printer,' which operates at a wavelength of 460 nm for cell-laden bioprinting experiments. Woodpile-shaped cell-scaffold structures were printed in cycles lasting 18–20 min (Fig. 6). As we demonstrated using the "ASIGA printer" (Figs. S8C–F), cells suspended in the ink before and after the printing process, were collected and cultured for 7 days (Fig. S9A), display similar viability and proliferation rates (Fig. S8C and Fig. S8E). After printing, the constructs were incubated to promote cell growth for up to 14 days. Microscopy imaging revealed that chondrocytes were embedded within the scaffold two days after printing, as shown in Fig. 6B. An MTS metabolic assay demonstrated cell viability within the scaffold at day 7, as illustrated in Fig. 6C. Additionally, cell viability was confirmed by Live/Dead staining at both 7 and 14 days post-printing (Fig. 6D and Fig. S9B).

4. Conclusion

In this work, a pristine gelatin solution was photopolymerized by Ru/SPS to fabricate 3D objects by DLP printing. Structures with different architectural complexities were successfully printed, including overhangs, open tubes, and detailed features, including hollow tubes. Ru/SPS transforms the dissolved gelatin into a crosslinked network by generating di-tyrosine bonds between the residues of two tyrosine amino acids. Therefore, the bioink is low-cost, as no chemical modification of the gelatin is required. This also decreases the risk of antigenicity responses for future biological applications. Additionally, we harness a new functionality of the dye Phenol red, which is used in cell culture media as a visual pH indicator; here, it functions as a photo-absorber pH visual indicator.

We demonstrated that complex 3D objects could be achieved using a typical DLP printer, reaching a high protein content of 30 wt% gelatin.

The printed object showed a compressive modulus of 31 kPa, which is in the region of soft tissues, relevant for the potential implantation use of the gelatin-based printed objects.

The biological results shown in the current study demonstrate the feasibility of using visible light-based 3D printing approaches to fabricate gelatin constructs for tissue engineering applications, specifically for engineering cartilage tissue. The results indicate that the 3D printed gelatin scaffolds support chondrocyte adhesion, survival, and proliferation, as evidenced by the cell-seeding experiments. Furthermore, the cell-laden printing approach, in which chondrocytes were incorporated directly within the gelatin formulation prior to printing, also enables maintaining cell viability and proliferative capacity for the tested durations.

The degradation profile of our crosslinked gelatin scaffold is critical to its potential biological applications. Based on previous studies with similar compositions, we estimate the degradation time of our crosslinked gelatin to be 3–4 weeks. This estimation is derived from Soliman et al. work [40], who reported a two-week degradation time for a similar but lower concentration gelatin ink. The higher gelatin concentration is expected to extend this degradation period. It is important to note that the degradation of native gelatin in physiological environments can vary. Ye et al. observed complete degradation of gelatin discs *in vivo* after 21 days [76], while Lukin et al. highlighted that degradation time depends on specific physiological conditions and enzyme presence [77]. Significantly, our crosslinked gelatin's estimated 3–4-week degradation time aligns well with the time scale for mature cartilage growth [78]. This matching allows for the potential tailoring of growing tissue's 3D structure with a gelatin-based scaffold, opening up possibilities for tissue engineering applications. The rationale of this study is to fabricate a scaffold with dual characteristics. On one hand, it has sufficient shape fidelity to fabricate complex 3D structures. On the other hand, its degradation profile is relatively short-term, enabling replacement by the cellular components (cells and ECM). The mature scaffold within the body is expected to gain mechanical stability from the biologically engineered tissue.

Overall, the formulation and printing process presented herein have the potential to revolutionize the use of non-modified protein-only bioinks for the fabrication of intricate 3D objects. This development is anticipated to open up new research avenues in biomedical engineering,

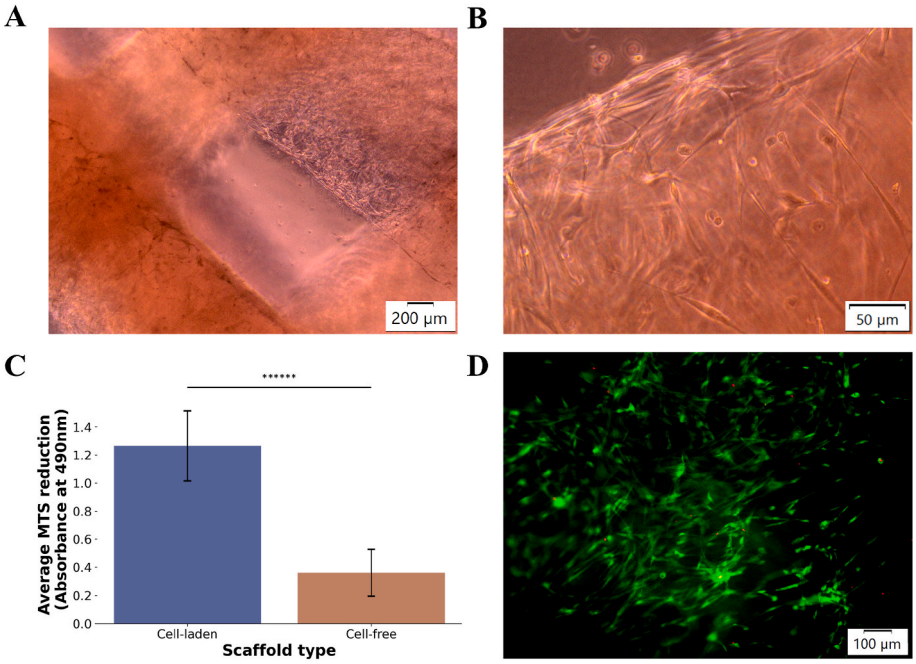

Fig. 6. Chondrocyte viability and growth within 3D printed cell-laden constructs. Chondrocytes were suspended within the bioink formulation and 3D printed. The woodpile-shaped printed constructs were grown in cell culture media for up to 7 days. (A, B) Bright-field microscopy images show embedded chondrocytes within the constructs presenting typical viable morphology. (C) MTS assay at day 7 post-printing demonstrates viability, N = 1, triplicate. Error bars represent standard deviation. (D) Overlayed microscopy image of Live (green)/Dead (red) dual staining performed with FDA/PI shows high cell viability rates. (For interpretation of the references to color in this figure legend, the reader is referred to the Web version of this article.)

making it possible to create previously unattainable structures with high fidelity and precision while using pristine proteins.

CRediT authorship contribution statement

Ayelet Bunin: Writing – review & editing, Writing – original draft, Investigation. **Orit Harari-Steinberg:** Writing – review & editing, Supervision, Conceptualization. **Doron Kam:** Writing – review & editing, Conceptualization. **Tatyana Kuperman:** Investigation. **Moran Friedman-Gohas:** Investigation. **Bruria Shalmon:** Investigation. **Liraz Larush:** Investigation. **Shay I. Duvdevani:** Writing – review & editing, Supervision, Conceptualization. **Shlomo Magdassi:** Writing – review & editing, Supervision, Conceptualization.

Data and materials availability

The data that support the findings of this study are openly available in the form of a Jupyter notebook in the FigShare repository at 10.6084/m9.figshare.25342954.

Declaration of generative AI and AI-assisted technologies in the writing process

During the preparation of this work, the authors used Grammarly, ChatGPT and Perplexity to improve language and readability. After using this tool, the authors reviewed and edited the content as needed and take full responsibility for the content of the publication.

Funding

This work was supported by the Israel Innovation Authority grants numbers 81144 and 81145.

Declaration of competing interest

The authors declare that they have no known competing financial interests or personal relationships that could have appeared to influence the work reported in this paper.

Acknowledgments

Ayelet Bunin thanks to the HUJI nano center M.Sc. program in Chemistry with specialization in Nanoscience and Nanotechnology. We also thank Prof. Ori Gidron and Yinon Deree for their help in the fluorescence experiments.

Appendix A. Supplementary data

Supplementary data to this article can be found online at https://doi.org/10.1016/j.mtbio.2024.101384.

Data availability

The data that support the findings of this study are openly available in the form of a Jupyter notebook in FigShare repository

References

[1] A. Al-Abboodi, S. Zhang, M. Al-Saady, J.W. Ong, P.P.Y. Chan, J. Fu, Printing in situ tissue sealant with visible-light-crosslinked porous hydrogel, Biomed. Mater. 14 (2019) 045010, https://doi.org/10.1088/1748-605X/AB19FE.

[2] M.J. Stoddart, E. Della Bella, A.R. Armiento, Cartilage tissue engineering: an introduction, in: Methods in Molecular Biology, 2022, pp. 1–7, https://doi.org/10.1007/978-1-0716-2839-3_1.

[3] H. Hong, Y.B. Seo, D.Y. Kim, J.S. Lee, Y.J. Lee, H. Lee, O. Ajiteru, M.T. Sultan, O. J. Lee, S.H. Kim, C.H. Park, Digital light processing 3D printed silk fibroin hydrogel for cartilage tissue engineering, Biomaterials 232 (2020) 119679, https://doi.org/10.1016/j.biomaterials.2019.119679.

[4] A.J.R. Amaral, V.M. Gaspar, P. Lavrador, J.F. Mano, Double network laminarin-boronic/alginate dynamic bioink for 3D bioprinting cell-laden constructs, Biofabrication 13 (2021), https://doi.org/10.1088/1758-5090/abfd79.

[5] B. Frost, B.P. Sutliff, P. Thayer, M.J. Bortner, E.J. Foster, Gradient poly(Ethylene glycol) diacrylate and cellulose nanocrystals tissue engineering composite scaffolds via extrusion bioprinting, Front. Bioeng. Biotechnol. 7 (2019), https://doi.org/10.3389/fbioe.2019.00280.

[6] M. Krishani, W.Y. Shin, H. Suhaimi, N.S. Sambudi, Development of scaffolds from bio-based natural materials for tissue regeneration applications: a review, Gels 9 (2023), https://doi.org/10.3390/gels9020100.

[7] X. Zhao, D.A. Hu, D. Wu, F. He, H. Wang, L. Huang, D. Shi, Q. Liu, N. Ni, M. Pakvasa, Y. Zhang, K. Fu, K.H. Qin, A.J. Li, O. Hagag, E.J. Wang, M. Sabharwal, W. Wagstaff, R.R. Reid, M.J. Lee, J.M. Wolf, M. El Dafrawy, K. Hynes, J. Strelzow, S.H. Ho, T.C. He, A. Athiviraham, Applications of biocompatible scaffold materials in stem cell-based cartilage tissue engineering, Front. Bioeng. Biotechnol. 9 (2021) 1–23, https://doi.org/10.3389/fbioe.2021.603444.

[8] M. Chen, Z. Jiang, X. Zou, X. You, Z. Cai, J. Huang, Advancements in tissue engineering for articular cartilage regeneration, Heliyon 10 (2024) e25400, https://doi.org/10.1016/j.heliyon.2024.e25400.

[9] M. Dufaud, L. Solé, M. Maumus, M. Simon, E. Perrier-Groult, G. Subra, C. Jorgensen, D. Noël, 3D bioprinting of articular cartilage: recent advances and perspectives, Bioprinting 28 (2022) e00253, https://doi.org/10.1016/j.bprint.2022.e00253.

[10] S. Landau, A.A. Szklanny, M. Machour, B. Kaplan, Y. Shandalov, I. Redenski, M. Beckerman, O. Harari-Steinberg, J. Zavin, O. Karni-Katovitch, I. Goldfracht, I. Michael, S.D. Waldman, S.I. Duvdevani, S. Levenberg, Human-engineered auricular reconstruction (hEAR) by 3D-printed molding with human-derived auricular and costal chondrocytes and adipose-derived mesenchymal stem cells, Biofabrication 14 (2022), https://doi.org/10.1088/1758-5090/ac3b91.

[11] J. Kundu, J.-H. Shim, J. Jang, S.-W. Kim, D.-W. Cho, An additive manufacturing-based PCL-alginate-chondrocyte bioprinted scaffold for cartilage tissue engineering, J Tissue Eng Regen Med 9 (2013) 1286–1297, https://doi.org/10.1002/term.1682.

[12] A. Kosik-Kozioł, M. Costantini, A. Mróz, J. Idaszek, M. Heljak, J. Jaroszewicz, E. Kijeńska, K. Szöke, N. Frerker, A. Barbetta, J.E. Brinchmann, W. Święszkowski, 3D bioprinted hydrogel model incorporating β-tricalcium phosphate for calcified cartilage tissue engineering, Biofabrication 11 (2019), https://doi.org/10.1088/1758-5090/ab15cb.

[13] O. A, C. Crowley, Z. M, E. P, M. A, Cartilage tissue engineering: the application of nanomaterials and stem cell technology, in: Tissue Engineering for Tissue and Organ Regeneration, InTech, 2011, https://doi.org/10.5772/22453.

[14] S. Schwarz, S. Kuth, T. Distler, C. Gögele, K. Stölzel, R. Detsch, A.R. Boccaccini, G. Schulze-Tanzil, 3D printing and characterization of human nasoseptal chondrocytes laden dual crosslinked oxidized alginate-gelatin hydrogels for cartilage repair approaches, Mater. Sci. Eng. C 116 (2020) 111189, https://doi.org/10.1016/j.msec.2020.111189.

[15] R.A. Buswell, W.R. Leal de Silva, S.Z. Jones, J. Dirrenberger, 3D printing using concrete extrusion: a roadmap for research, Cement Concr. Res. 112 (2018) 37–49, https://doi.org/10.1016/J.CEMCONRES.2018.05.006.

[16] Z. Zheng, D. Eglin, M. Alini, G.R. Richards, L. Qin, Y. Lai, Visible light-induced 3D bioprinting technologies and corresponding bioink materials for tissue engineering: a review, Engineering 7 (2021) 966–978, https://doi.org/10.1016/J.ENG.2020.05.021.

[17] J. Shi, B. Wu, S. Li, J. Song, B. Song, W.F. Lu, Shear stress analysis and its effects on cell viability and cell proliferation in drop-on-demand bioprinting, Biomed Phys Eng Express 4 (2018), https://doi.org/10.1088/2057-1976/aac946.

[18] A. Bhusal, E. Dogan, H.A. Nguyen, O. Labutina, D. Nieto, A. Khademhosseini, A. K. Miri, Multi-material digital light processing bioprinting of hydrogel-based microfluidic chips, Biofabrication 14 (2022), https://doi.org/10.1088/1758-5090/ac2d78.

[19] H. Goodarzi Hosseinabadi, A. Biswas, A. Bhusal, A. Yousefinejad, A. Lall, W. H. Zimmermann, A.K. Miri, L. Ionov, 4D-Printable photocrosslinkable polyurethane-based inks for tissue scaffold and actuator applications, Small 20 (2024) 1–13, https://doi.org/10.1002/smll.202306387.

[20] H. Goodarzi Hosseinabadi, E. Dogan, A.K. Miri, L. Ionov, Digital light processing bioprinting advances for microtissue models, ACS Biomater. Sci. Eng. 8 (2022) 1381–1395, https://doi.org/10.1021/acsbiomaterials.1c01509.

[21] W. Li, M. Wang, H. Ma, F.A. Chapa-Villarreal, A.O. Lobo, Y.S. Zhang, Stereolithography apparatus and digital light processing-based 3D bioprinting for tissue fabrication, iScience 26 (2023) 106039, https://doi.org/10.1016/j.isci.2023.106039.

[22] Z. Yazdanpanah, J.D. Johnston, D.M.L. Cooper, X. Chen, 3D bioprinted scaffolds for bone tissue engineering: state-of-the-art and emerging technologies, Front. Bioeng. Biotechnol. 10 (2022) 418, https://doi.org/10.3389/FBIOE.2022.824156/BIBTEX.

[23] W. Li, L.S. Mille, J.A. Robledo, T. Uribe, V. Huerta, Y.S. Zhang, Recent advances in formulating and processing biomaterial inks for vat polymerization-based 3D printing, Adv. Healthcare Mater. 9 (2020) 2000156, https://doi.org/10.1002/ADHM.202000156.

[24] W. Li, L.S. Mille, J.A. Robledo, T. Uribe, V. Huerta, Y.S. Zhang, Recent advances in formulating and processing biomaterial inks for vat polymerization-based 3D printing, Adv. Healthcare Mater. 9 (2020) 2000156, https://doi.org/10.1002/ADHM.202000156.

[25] X. Mu, F. Agostinacchio, N. Xiang, Y. Pei, Y. Khan, C. Guo, P. Cebe, A. Motta, D. L. Kaplan, Recent advances in 3D printing with protein-based inks, Prog. Polym. Sci. 115 (2021) 101375, https://doi.org/10.1016/j.progpolymsci.2021.101375.

[26] X. Mu, J.K. Sahoo, P. Cebe, D.L. Kaplan, Photo-crosslinked silk fibroin for 3d printing, Polymers 12 (2020) 1–18, https://doi.org/10.3390/polym12122936.
[27] K. Chen, Y. Feng, Y. Zhang, L. Yu, X. Hao, F. Shao, Z. Dou, C. An, Z. Zhuang, Y. Luo, Y. Wang, J. Wu, P. Ji, T. Chen, H. Wang, Entanglement-driven adhesion, self-healing, and high stretchability of double-network PEG-based hydrogels, ACS Appl. Mater. Interfaces 11 (2019) 36458–36468, https://doi.org/10.1021/ACSAMI.9B14348/SUPPL_FILE/AM9B14348_SI_002.MP4.
[28] A. Bahar, R. Rusijono, N. Kusumawati, Extraction and characterization of the base halal gelatin based on bovine, Bone 171 (2018) 46–49, https://doi.org/10.2991/snk-18.2018.10.
[29] S. Petros, T. Tesfaye, M. Ayele, A review on gelatin based hydrogels for medical textile applications, J. Eng. 2020 (2020), https://doi.org/10.1155/2020/8866582.
[30] S. Chatterjee, P. Chi-leung Hui, Review of stimuli-responsive polymers in drug delivery and textile application, Molecules 24 (2019) 2547, https://doi.org/10.3390/molecules24142547.
[31] Y. Wang, M. Ma, J. Wang, W. Zhang, W. Lu, Y. Gao, B. Zhang, Y. Guo, Development of a photo-crosslinking, biodegradable GelMA/PEGDA hydrogel for guided bone regeneration materials, Materials 11 (2018) 1345, https://doi.org/10.3390/MA11081345, 1345 11 (2018).
[32] S. Chen, Q. Zhang, T. Nakamoto, N. Kawazoe, G. Chen, Gelatin scaffolds with controlled pore structure and mechanical property for cartilage tissue engineering, Tissue Eng. C Methods 22 (2016) 189–198, https://doi.org/10.1089/ten.tec.2015.0281.
[33] A. Maihemuti, H. Zhang, X. Lin, Y. Wang, Z. Xu, D. Zhang, Q. Jiang, 3D-printed fish gelatin scaffolds for cartilage tissue engineering, Bioact. Mater. 26 (2023) 77–87, https://doi.org/10.1016/j.bioactmat.2023.02.007.
[34] H.W. Liu, W.T. Su, C.Y. Liu, C.C. Huang, Highly organized porous gelatin-based scaffold by microfluidic 3D-foaming technology and dynamic culture for cartilage tissue engineering, Int. J. Mol. Sci. 23 (2022), https://doi.org/10.3390/ijms23158449.
[35] Q. Ge, Z. Chen, J. Cheng, B. Zhang, Y.F. Zhang, H. Li, X. He, C. Yuan, J. Liu, S. Magdassi, S. Qu, 3D printing of highly stretchable hydrogel with diverse UV curable polymers, Sci. Adv. 7 (2021) 1–11, https://doi.org/10.1126/sciadv.aba4261.
[36] A.A. Pawar, G. Saada, I. Cooperstein, L. Larush, J.A. Jackman, S.R. Tabaei, N.-J. Cho, S. Magdassi, High-performance 3D printing of hydrogels by water-dispersible photoinitiator nanoparticles, Sci. Adv. 2 (2016) 1–8, https://doi.org/10.1126/sciadv.1501381.
[37] C.M. Elvin, T. Vuocolo, A.G. Brownlee, L. Sando, M.G. Huson, N.E. Liyou, P. R. Stockwell, R.E. Lyons, M. Kim, G.A. Edwards, G. Johnson, G.A. McFarland, J.A. M. Ramshaw, J.A. Werkmeister, A highly elastic tissue sealant based on photopolymerised gelatin, Biomaterials 31 (2010) 8323–8331, https://doi.org/10.1016/j.biomaterials.2010.07.032.
[38] P.G. Parsons, P. Goss, Chromosome damage and DNA repair induced in human fibroblasts by UV and cholesterol oxide, Aust. J. Exp. Biol. Med. Sci. 56 (1978) 287–296, https://doi.org/10.1038/ICB.1978.30.
[39] G. Sun, Y. Huang, J. Ma, D. Li, Q. Fan, Y. Li, J. Shao, Photoinitiation mechanisms and photogelation kinetics of blue light induced polymerization of acrylamide with bicomponent photoinitiators, J. Polym. Sci. 59 (2021) 567–577, https://doi.org/10.1002/pol.20200818.
[40] B.G. Soliman, A. Longoni, M. Wang, W. Li, P.N. Bernal, A. Cianciosi, G.C. J. Lindberg, J. Malda, J. Groll, T. Jungst, R. Levato, J. Rnjak-Kovacina, T.B. F. Woodfield, Y.S. Zhang, K.S. Lim, Programming delayed dissolution into sacrificial bioinks for dynamic temporal control of architecture within 3D-bioprinted constructs, Adv. Funct. Mater. 33 (2023), https://doi.org/10.1002/adfm.202210521.
[41] K.S. Lim, R. Levato, P.F. Costa, M.D. Castilho, C.R. Alcala-Orozco, K.M.A. Van Dorenmalen, F.P.W. Melchels, D. Gawlitta, G.J. Hooper, J. Malda, T.B. F. Woodfield, Bio-resin for high resolution lithography-based biofabrication of complex cell-laden constructs, Biofabrication 10 (2018) 034101, https://doi.org/10.1088/1758-5090/aac00c.
[42] Q. Mao, Y. Wang, Y. Li, S. Juengpanich, W. Li, M. Chen, J. Yin, J. Fu, X. Cai, Fabrication of liver microtissue with liver decellularized extracellular matrix (dECM) bioink by digital light processing (DLP) bioprinting, Mater. Sci. Eng. C 109 (2020), https://doi.org/10.1016/J.MSEC.2020.110625.
[43] D. Kam, A. Olender, A. Rudich, Y. Kan-Tor, A. Buxboim, O. Shoseyov, S. Magdassi, 3D printing of resilin in water by multiphoton absorption polymerization, Adv. Funct. Mater. 2210993 (2022), https://doi.org/10.1002/adfm.202210993.
[44] M. Xie, L. Lian, X. Mu, Z. Luo, C.E. Garciamendez-Mijares, Z. Zhang, A. López, J. Manríquez, X. Kuang, J. Wu, J.K. Sahoo, F.Z. González, G. Li, G. Tang, S. Maharjan, J. Guo, D.L. Kaplan, Y.S. Zhang, Volumetric additive manufacturing of pristine silk-based (bio)inks, Nat. Commun. 14 (2023), https://doi.org/10.1038/s41467-023-35807-7.
[45] J.K. Placone, J. Navarro, G.W. Laslo, M.J. Lerman, A.R. Gabard, G.J. Herendeen, E. E. Falco, S. Tomblyn, L. Burnett, J.P. Fisher, Development and characterization of a 3D printed, keratin-based hydrogel, Ann. Biomed. Eng. 45 (2017) 237–248, https://doi.org/10.1007/s10439-016-1621-7.
[46] D. Shin, J. Hyun, Silk fibroin microneedles fabricated by digital light processing 3D printing, J. Ind. Eng. Chem. 95 (2021) 126–133, https://doi.org/10.1016/j.jiec.2020.12.011.
[47] S. Sakai, H. Ohi, M. Taya, Gelatin/hyaluronic acid content in hydrogels obtained through blue light-induced gelation affects hydrogel properties and adipose stem cell behaviors, Biomolecules 9 (2019), https://doi.org/10.3390/biom9080342.
[48] W. Li, M. Wang, L.S. Mille, J.A. Robledo Lara, V. Huerta, T. Uribe Velázquez, F. Cheng, H. Li, J. Gong, T. Ching, C.A. Murphy, A. Lesha, S. Hassan, T.B. F. Woodfield, K.S. Lim, Y.S. Zhang, A smartphone-enabled portable digital light processing 3D printer, Adv. Mater. 33 (2021) 1–10, https://doi.org/10.1002/adma.202102153.
[49] K.S. Lim, B.S. Schon, N.V. Mekhileri, G.C.J. Brown, C.M. Chia, S. Prabakar, G. J. Hooper, T.B.F. Woodfield, New visible-light photoinitiating system for improved print fidelity in gelatin-based bioinks, ACS Biomater. Sci. Eng. 2 (2016) 1752–1762, https://doi.org/10.1021/acsbiomaterials.6b00149.
[50] C. Lu, K. Deng, A. Porter, K. Kelvin Fu, Top-down digital light processing 3D printing of composite structures using carbon fiber modified UV curable resin, Adv. Compos. Hybrid Mater. 6 (2023) 1–8, https://doi.org/10.1007/s42114-022-00605-0.
[51] K. Kato, Y. Ikeda, K. Ito, Direct determination of cross-link density and its correlation with the elastic modulus of a gel with slidable cross-links, ACS Macro Lett. 8 (2019) 700–704, https://doi.org/10.1021/acsmacrolett.9b00238.
[52] Y. Li, B. Sun, Y. Liu, Z. Zhang, Y. Shen, H. Wang, X. Liu, W. Xie, Evaluation of effective crosslinking density for pseudo-semi interpenetrating polymer networks based on polyether glycols mixture by dynamic mechanical analysis, Polymers 15 (2023), https://doi.org/10.3390/polym15010226.
[53] J.Y. Lai, L.J. Luo, D.H.K. Ma, Effect of cross-linking density on the structures and properties of carbodiimide-treated gelatin matrices as limbal stem cell niches, Int. J. Mol. Sci. 19 (2018) 1–21, https://doi.org/10.3390/ijms19113294.
[54] B. Elysée-Collen, R.W. Lencki, Protein ternary phase diagrams. 1. Effect of ethanol, ammonium sulfate, and temperature on the phase behavior of type B gelatin, J. Agric. Food Chem. 44 (1996) 1651–1657, https://doi.org/10.1021/jf950676r.
[55] C. Megan Mae, R. Dave Arthur R, An investigation on the effects of varying temperatures on gelatin denaturation in response to enzymatic reactions from fruit extracts, Journal of Industrial Biotechnology 3 (2022) 10–18, https://doi.org/10.36959/967/629.
[56] T.H. Donnelly, F.L. Kauffman, P. Arendovich, Molecular changes in the high-temperature degradation of gelatin, J. Polym. Sci. Part C: Polymer Symposia 23 (1968) 79–86, https://doi.org/10.1002/polc.5070230111.
[57] X. Jiang, S. Lyu, M. Ali, J. Huang, W. Jiang, Z. Qiu, Q. Sui, Enhancement of benzene degradation by persulfate oxidation: synergistic effect by nanoscale zero-valent iron (nZVI) and thermal activation, Water Sci. Technol. 82 (2020) 998–1008, https://doi.org/10.2166/wst.2020.408.
[58] X. Cui, B.G. Soliman, C.R. Alcala-Orozco, J. Li, M.A.M. Vis, M. Santos, S.G. Wise, R. Levato, J. Malda, T.B.F. Woodfield, J. Rnjak-Kovacina, K.S. Lim, Rapid photocrosslinking of silk hydrogels with high cell density and enhanced shape fidelity, Adv. Healthcare Mater. 9 (2020) 1–15, https://doi.org/10.1002/adhm.201901667.
[59] P.F. Jacobs, Rapid prototyping & manufacturing— fundamentals of stereolithography, J. Manuf. Syst. 12 (1993) 430–433, https://doi.org/10.1016/0278-6125(93)90311-g.
[60] P.F. Jacobs, Rapid prototyping & manufacturing— fundamentals of stereolithography, J. Manuf. Syst. 12 (1993) 430–433, https://doi.org/10.1016/0278-6125(93)90311-g.
[61] Y. Ma, W. Wei, L. Gong, C. Li, Y. Hong, X. Wang, R. Liang, Q. Shao, Q. Liang, W. Huang, M.J. Shipston, H. Ouyang, Biomacromolecule-based agent for high-precision light-based 3D hydrogel bioprinting, Cell Rep Phys Sci 3 (2022) 100985, https://doi.org/10.1016/j.xcrp.2022.100985.
[62] M. Leulescu, A. Rotaru, I. Pălărie, A. Moanță, N. Cioateră, M. Popescu, E. Morîntale, M.V. Bubulică, G. Florian, A. Hărăbor, P. Rotaru, Tartrazine: physical, thermal and biophysical properties of the most widely employed synthetic yellow food-colouring azo dye, J. Therm. Anal. Calorim. 134 (2018) 209–231, https://doi.org/10.1007/s10973-018-7663-3.
[63] S.C. Ligon, R. Liska, J. Stampfl, M. Gurr, R. Mülhaupt, Polymers for 3D printing and customized additive manufacturing, Chem. Rev. 117 (2017) 10212–10290, https://doi.org/10.1021/acs.chemrev.7b00074.
[64] K. Arcaute, B.K. Mann, R.B. Wicker, Stereolithography of three-dimensional bioactive poly(ethylene glycol) constructs with encapsulated cells, Ann. Biomed. Eng. 34 (2006) 1429–1441, https://doi.org/10.1007/s10439-006-9156-y.
[65] J. Fouassier, Dyes and Chromophores in Polymer Science, John Wiley & Sons, Ltd, 2015.
[66] N. Corrigan, J. Yeow, P. Judzewitsch, J. Xu, C. Boyer, Seeing the light: advancing materials Chemistry through photopolymerization, Angew. Chem. Int. Ed. 58 (2019) 5170–5189, https://doi.org/10.1002/anie.201805473.
[67] D.A. Malencik, S.R. Anderson, Dityrosine as a product of oxidative stress and fluorescent probe, Amino Acids 25 (2003) 233–247, https://doi.org/10.1007/s00726-003-0014-z.
[68] GMIA, Gelatin Handbook, 2019.
[69] C. Chen, M. Zhang, A.S. Mujumdar, P. Phuhongsung, Investigation of 4D printing of lotus root-compound pigment gel: effect of pH on rapid colour change, Food Res. Int. 148 (2021) 110630, https://doi.org/10.1016/j.foodres.2021.110630.
[70] A.F. Ghazal, M. Zhang, B. Bhandari, H. Chen, Investigation on spontaneous 4D changes in color and flavor of healthy 3D printed food materials over time in response to external or internal pH stimulus, Food Res. Int. 142 (2021) 110215, https://doi.org/10.1016/j.foodres.2021.110215.
[71] F. Tsegay, M. Hisham, M. Elsherif, A. Schiffer, H. Butt, 3D printing of pH indicator auxetic hydrogel skin wound dressing, Molecules 28 (2023) 1–18, https://doi.org/10.3390/molecules28031339.
[72] A. Kostelnik, A. Cegan, M. Pohanka, Color change of phenol red by integrated smart phone camera as a tool for the determination of neurotoxic compounds, Sensors 16 (2016), https://doi.org/10.3390/s16091212.
[73] A.D. Drozdov, J. de C. Christiansen, Tension–compression asymmetry in the mechanical response of hydrogels, J. Mech. Behav. Biomed. Mater. 110 (2020) 103851, https://doi.org/10.1016/j.jmbbm.2020.103851.

[74] R. Ferraro, S. Guido, S. Caserta, M. Tassieri, Compressional stress stiffening & softening of soft hydrogels - how to avoid artefacts in their rheological characterisation, Soft Matter 19 (2023) 2053–2057, https://doi.org/10.1039/d3sm00077j.
[75] K.O. Rojek, M. Ćwiklińska, J. Kuczak, J. Guzowski, Microfluidic formulation of topological hydrogels for microtissue engineering, Chem. Rev. 122 (2022) 16839–16909, https://doi.org/10.1021/acs.chemrev.1c00798.
[76] Q. Ye, M.C. Harmsen, Y. Ren, R.A. Bank, The role of collagen receptors Endo180 and DDR-2 in the foreign body reaction against non-crosslinked collagen and gelatin, Biomaterials 32 (2011) 1339–1350, https://doi.org/10.1016/j.biomaterials.2010.09.076.
[77] I. Lukin, I. Erezuma, L. Maeso, J. Zarate, M.F. Desimone, T.H. Al-Tel, A. Dolatshahi-Pirouz, G. Orive, Progress in gelatin as biomaterial for tissue engineering, Pharmaceutics 14 (2022) 1–19, https://doi.org/10.3390/pharmaceutics14061177.
[78] I.S. Park, R.L. Jin, H.J. Oh, M.D. Truong, B.H. Choi, S.H. Park, D.Y. Park, B.H. Min, Sizable scaffold-free tissue-engineered articular cartilage construct for cartilage defect repair, Artif. Organs 43 (2019) 278–287, https://doi.org/10.1111/aor.13329.